



# Influence of austenitisation temperatures during hot stamping on the local electrochemical behaviour of 22MnB5 steel coated with hot-dip Al-Si

Camila Pucci Couto<sup>a,b,c,\*</sup>, Reynier I. Revilla<sup>b</sup>, Rodolfo Politano<sup>a</sup>, Isolda Costa<sup>a</sup>, Zehbour Panossian<sup>c</sup>, Iris De Graeve<sup>b</sup>, Jesualdo Luiz Rossi<sup>a</sup>, Herman Terry<sup>b</sup>

<sup>a</sup> Nuclear and Energy Research Institute, Materials Science and Technology Centre, Av. Prof. Lineu Prestes 2242, 05508-000, São Paulo, Brazil

<sup>b</sup> Vrije Universiteit Brussel, Department of Chemistry and Materials, Research Group of Electrochemical and Surface Engineering, Pleinlaan 2, 1050, Brussels, Belgium

<sup>c</sup> Institute for Technological Research, Laboratory for Corrosion and Protection, Av. Prof. Almeida Prado 532, 05508-901, São Paulo, Brazil

## ARTICLE INFO

### Keywords:

Hot stamping  
Austenitisation temperature  
Hot-dip Al-Si  
Electrochemical behaviour  
Scanning kelvin probe force microscopy

## ABSTRACT

Scanning Kelvin probe force microscopy was used to evaluate the effect of austenitisation temperatures during hot stamping on the local electrochemical behaviour of 22MnB5 steel coated with hot-dip Al-Si. A variation in the austenitisation temperature around 50 °C substantially altered the coating morphology as well as the local electrochemical behaviour of the system (coating/steel). Both coating layer and steel substrate became nobler as the austenitisation temperature increased. The former was due to the overall iron enrichment while the latter was related to the microstructural transformation during quenching. Therefore, the driving force for cathodic protection decreased as the austenitisation temperature increased.

## 1. Introduction

The widespread use of hot-stamped components in the automotive industry can be related to their advantages in terms of lightweight and crashworthiness ratio [1–3]. The hot-stamping technology allows the production of complex design components of ultra-high strength steels without the influence of springback effect [4–6]. The springback is a phenomenon related to the mechanical working of ultra or high-strength steels at room temperature [6–8]. This affects mostly the final design and dimensions of the formed component. Consequently, ultra or high-strength structural components have been produced by means of hot stamping [9]. The direct hot-stamping process consists of heating up the steel blank at austenitisation temperatures and then transferring it from the furnace to the press tool for simultaneous forming and quenching [6,8,10–12].

The boron-manganese steel, 22MnB5 grade, has been the most used in the industry for hot-stamping applications due to its high hardenability. This is an intrinsic property related to the steel composition, greatly influenced by carbon, manganese and boron content addition [4, 5,8,13–15]. Before hot stamping, the steel has a ferrite-pearlite microstructure and tensile strength around 600 MPa; at the end of the process, the tensile strength may increase up to 1500 MPa, due to martensitic

transformation which takes place during the quenching [4,6,9,15].

In order to avoid both steel oxidation and decarburisation, the substrate is usually protected with a metallic coating before hot stamping [6,8]. The hot-dip aluminium-silicon (Si 10 % in mass fraction) is the main metallic coating applied for hot stamping [6,10,11,16]. The Al-Si system has already been used in exhaust systems due to its resistance to both corrosion and oxidation at high temperatures, due to the presence of a dense and stable oxide layer [17,18]. However, the thermo-mechanical process changes the coating morphology as a consequence of iron, aluminium and silicon diffusion which occurs at high temperatures [16,19,20].

The electrochemical behaviour of the hot-stamped steel coated with Al-Si coating has been evaluated by means of global and local electrochemical techniques [10,11,21,22]. The necessity for local investigations has been highlighted by the complexity of the system composed of several layers which present different intermetallic phases [21,22]. In a previous investigation, the effect of hot-stamping process on the electrochemical behaviour of 22MnB5 steel coated with Al-Si (Si 10 % in mass fraction) was evaluated by means of scanning Kelvin probe force microscopy (SKPFM). The results showed that the iron enrichment in the coating layer during austenitisation leads to the coating ennoblement and reduction of the driving force for cathodic protection, as the

\* Corresponding author at: Nuclear and Energy Research Institute, Materials Science and Technology Centre, Av. Prof. Lineu Prestes 2242, 05508-000, São Paulo, Brazil.

E-mail addresses: [camila.puccicouto@usp.br](mailto:camila.puccicouto@usp.br), [Camila.Pucci.Couto@vub.be](mailto:Camila.Pucci.Couto@vub.be) (C.P. Couto).

<https://doi.org/10.1016/j.corsci.2021.109673>

Received 14 April 2021; Received in revised form 14 June 2021; Accepted 6 July 2021

Available online 8 July 2021

0010-938X/© 2021 Elsevier Ltd. All rights reserved.

Volta-potential difference between the steel substrate and the coating layer greatly decreased [21]. However, the samples used in the referred work [21] were provided by a carmaker, therefore, the process parameters, such as austenitisation temperature, soaking time and cooling rate were not known.

It is known that the coating morphology is highly influenced by the process parameters during hot stamping [16,19,20]. Windmann et al. [19,20] have shown that increasing the soaking temperature increases the growth of ductile intermetallic phases in the coating layer, as the iron diffusion is promoted. Nonetheless, little is known about the influence that these process parameters could have on the electrochemical behaviour of the system (coating/steel). Therefore, this work aims at correlating the effect of austenitisation temperatures during hot stamping on the morphology of the Al-Si coating with the local electrochemical properties of this system. Samples of 22MnB5 steel coated with hot-dip Al-Si (Si 10 % in mass fraction) were prepared at different austenitisation temperatures, maintaining the soaking time constant. Microstructural analysis was carried out using field emission-scanning electron microscopy (FE-SEM) and energy dispersive X-ray spectroscopy (EDS). Additionally, surface potential maps of the coatings' cross sections were studied by means of scanning Kelvin probe force microscopy (SKPFM). Despite the similarity with our previous work [21], this approach allowed a better understanding the galvanic interactions within the coating layer and between the coating and the metal substrate as function of the austenitisation temperature.

## 2. Experimental

### 2.1. Samples

Blanks of 22MnB5 steel with a thickness of 1.4 mm and hot-dip coated with Al-Si (Si 10 % in mass fraction) were submitted to a hot-stamping process on laboratory scale. The coating has an average thickness of 25  $\mu\text{m}$  per side and mass of 150  $\text{g} \cdot \text{m}^{-2}$  double-sided [23]. The samples were heated up at different austenitisation temperatures (850  $^{\circ}\text{C}$ , 900  $^{\circ}\text{C}$  and 950  $^{\circ}\text{C}$ ) for 8 min. The transfer time from the furnace to the press tool was lower than 7 s. The stamping tool was composed of a cooling system by water ducts with flow rate of 13  $\text{L} \cdot \text{min}^{-1}$  and the ducts temperature were maintained at 5  $^{\circ}\text{C}$ . The press tool had a clamping force of 79 t and a contact pressure was maintained at 70 MPa. There was no mechanical deformation of the specimens; there was only compressive strain, as they were kept flat. During hot stamping, the microstructure of the steel substrate is transformed from ferrite-pearlite into martensite.

After hot stamping, the specimens were cut into small samples suitable for electrochemical measurements and surface characterisations. The hot dipped and heat-treated surface (30  $\times$  30  $\text{mm}^2$ ) was cleaned in isopropanol and dried by a cold stream of air. Cross-section polished samples were prepared by hot mounting in Bakelite, grinding and polishing with 0.25  $\mu\text{m}$  colloidal silica suspension as the final step. In this work, the samples before hot stamping were named as "AR" (as received) whereas the samples submitted to the press hardening were designated as "PHS" (press-hardened steel), as shown in Table 1.

### 2.2. Cross-section characterisation

The characterisation of AR and PHS sample cross-sections were

**Table 1**  
Steel samples' identification and their corresponding experimental conditions.

Sample ID	Condition
AR	22MnB5 coated with hot-dip Al-Si (10 %Si in mass fraction)
PHS850	AR condition heated at 850 $^{\circ}\text{C}$ for 8 min and hot stamped
PHS900	AR condition heated at 900 $^{\circ}\text{C}$ for 8 min and hot stamped
PHS950	AR condition heated at 950 $^{\circ}\text{C}$ for 8 min and hot stamped

carried out using a field emission-scanning electron microscope (FE-SEM). FE-SEM images were obtained in backscattering mode, using 15 kV acceleration voltage of 30 pA probe current and a work distance of 10 mm. The mappings of the chemical composition and the local quantitative analyses (point ID) were obtained by means of energy dispersive X-ray spectroscopy (EDS).

### 2.3. Electrochemical measurements and scanning Kelvin probe force microscopy

Electrochemical tests were carried out using a three-electrode cell configuration consisting of an Ag|AgCl| 3  $\text{mol} \cdot \text{L}^{-1}$  KCl as a reference electrode (RE), a platinum grid as counter electrode (CE) and the sample as working electrode (WE). The open circuit potential (OCP) was measured in aerated 5.0 % NaCl (in mass fraction) for 1 h. After OCP measurements, anodic polarisation curves were obtained, starting from 200 mV below the OCP with a sweep rate of 1  $\text{mV} \cdot \text{s}^{-1}$ . All tests were carried out at room temperature and the working electrode surface was a circular region with 1 cm in diameter. At least three measurements were carried out for each sample condition. The average values and the standard deviation of open circuit potential (OCP), at  $t = 3600$  s, and corrosion potential ( $E^*$ ) were calculated.

The samples' topographies, Volta-potential mappings and their respective Volta-potential line profile were recorded by scanning Kelvin probe force microscopy (SKPFM) with a commercial atomic force microscope (Park Systems XE-100). These measurements were performed under ambient conditions using rectangular conductive cantilevers with a Pt/Ir coating, a resonant frequency of 50 kHz–70 kHz and a spring constant of 1  $\text{N} \cdot \text{m}^{-1}$  to 5  $\text{N} \cdot \text{m}^{-1}$ . Additionally, highly oriented pyrolytic graphite (HOPG) was used as a reference material for the calibration of the measured Volta potential for each sample. Topographic and corresponding potential images were simultaneously gained using a dynamic mode with a single-pass methodology. This methodology is based on frequency modulation mode, in which distance-related artefacts are eliminated. The potential signal recorded was inverted in order to reflect the real relation between the Volta-potential values of the surface under investigation [17,24–26]. In the Volta-potential mappings the darkest contrast is related to the most anodic phase whereas the brightest contrast to the most cathodic one. Furthermore, the distribution of Volta-potential was represented by means of histograms. The histograms were constructed based on the Volta-potential map, correspondent to a scanned area of 40  $\times$  40  $\mu\text{m}^2$  which corresponded to a mapping of 512 pixels  $\times$  512 pixels. Each pixel represents a potential value. Therefore, each histogram is constructed with 512  $\times$  512 values of potential. Finally, from the histograms is possible to calculate the average Volta potential of each constituent present in the sample, based on the following steps:

- 1 Determining the limit of the potential for each constituent (e.g., coating layer) and then, separating the data (of the coating layer) related to potential and the number of counts;
- 2 Sum of the counts;
- 3 Multiply each value of potential by its corresponding number of count;
- 4 Sum of the results from step 3;
- 5 Divide the results of step 4 by the value of the sum of the counts (step 2); the result is the average potential.

## 3. Results and discussion

### 3.1. Cross-section coating characterisation as function of different austenitisation temperatures

Fig. 1 shows the effect of the different austenitisation temperatures on the Al-Si coating morphology while Fig. 2 shows the EDS data (Fig. 2 (a)) and individual cross sectional mappings of the elements (Fig. 2

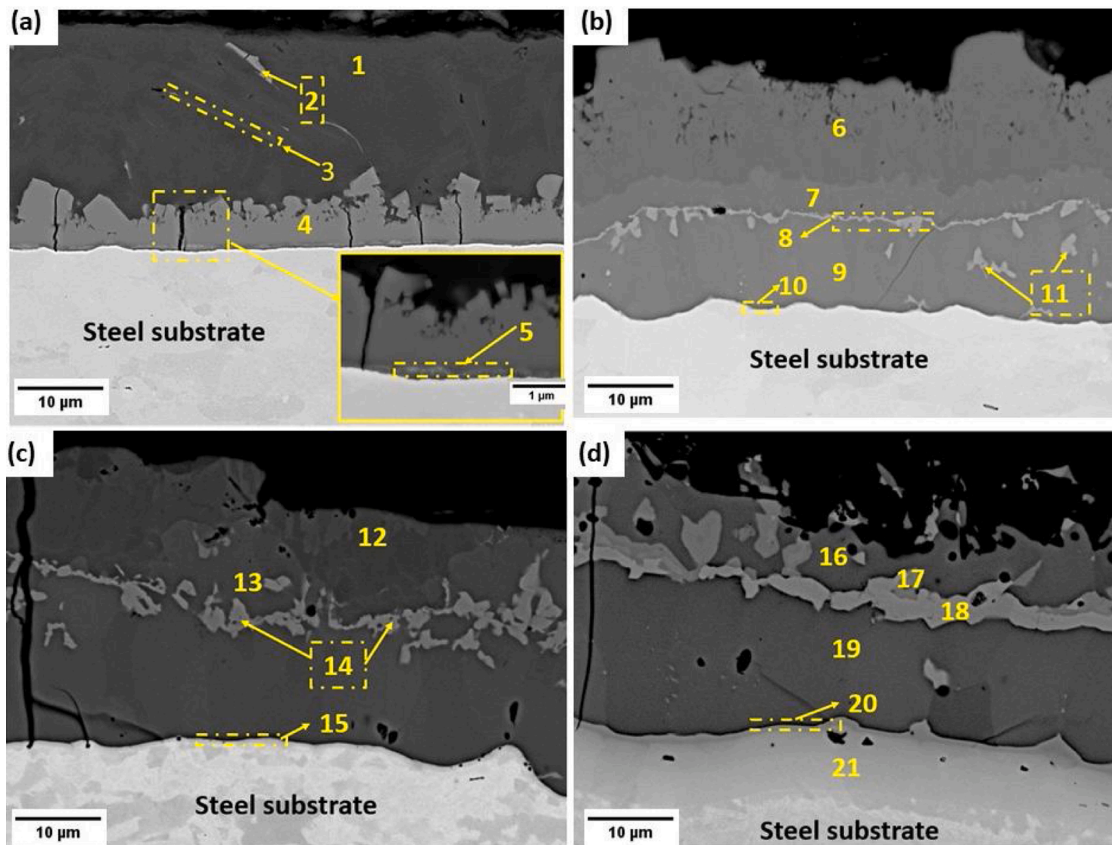


Fig. 1. Scanning backscattered electron images showing the cross-section morphologies of 22MnB5 steel coated with hot-dip Al-Si (10 % Si in mass fraction) in different conditions highlighting the different intermetallic phases present in: (a) AR; (b) PHS850; (c) PHS900; and (d) PHS950.

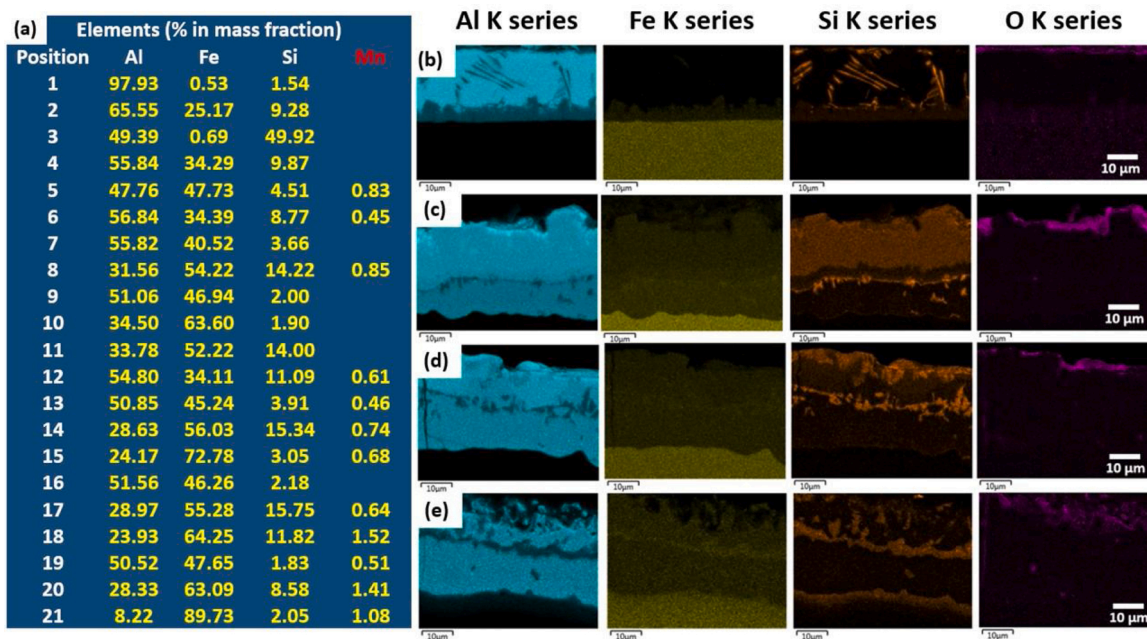


Fig. 2. EDS analyses: (a) punctual identification for the positions highlighted in Fig. 1; and EDS elemental mappings for Al, Fe, Si and O of (b) AR; (c) PHS850; (d) PHS900; (e) PHS950.

(b–e)). The cross-section morphology of AR, before hot stamping, is shown in Fig. 1 (a). The coating consists of an aluminium matrix (spot 1) and some precipitates (spots 2 and 3). The precipitates are characterised as either Al-Fe-Si (2) or Si (3). In addition to this, there is also an

interdiffusion layer present (region 4) which shows a similar composition as the ternary precipitates (spot 2). The interdiffusion layer (IDL) is composed of two sublayers known as upper interdiffusion layer (UIDL) and lower interdiffusion layer (LIDL) [17]. The LIDL is thin and bright,

adjacent to the steel substrate and enriched in iron (spot 5).

Micro cracks can be identified in the IDL (Fig. 1 (a)) which are correlated with the formation of the LIDL, reported as a brittle phase ( $\eta$ -Fe<sub>2</sub>Al<sub>5</sub>) [17,26]. The silicon addition has been pointed out as an alternative to suppress the growth of the LIDL and to promote the growth of the more ductile UIDL, which consists of a mixture of intermetallics, such as  $\theta$ -FeAl<sub>3</sub> and  $\tau_5$ -Al<sub>7</sub>Fe<sub>2</sub>Si [17,18,24–26]. Moreover, the relatively smooth interface between the steel substrate and the coating layer is also an effect of the silicon content. In pure hot-dip aluminised steels, this interface shows a finger-like structure which can enhance the formation of cracks and coating delamination [17,18,26]. The EDS mapping for oxygen (Fig. 2 (b)) shows its enrichment at the top surface related to the native oxide layer.

The effect of austenitisation at 850 °C for 8 min on the Al-Si coating layer is seen in Fig. 1 (b) and Fig. 2 (c) for the PHS850 sample. The backscattered electron image displays different contrasts for the present phases, indicating different compositions. The top coating (spot 6) consists of a ternary Al-Fe-Si phase being enriched in aluminium, while its underlayer (spot 7) is basically composed of Al-Fe phase, since the silicon content is very little, as shown in both point ID and EDS mappings analyses (Fig. 2 (a) and Fig. 2 (c)). Conversely, the highest silicon content is seen in the thin and bright layer (spot 8) which is a ternary Al-Fe-Si phase (Si about 14 % in mass fraction). This same phase is also seen as an island morphology (spot 11) close to the steel substrate. The silicon content significantly decreases towards the steel substrate, while the iron content increases. There is a thin layer (spot 10) at the interface between the coating layer and the steel substrate which has a high iron content. This can be considered as the interdiffusion layer for this sample condition. In general, the iron content gradually decreases from the steel substrate towards the coating top surface. The EDS maps (Fig. 2 (c)) show the presence of an oxide layer at the coating top surface. This layer seems to be thicker than the one seen on the surface of the AR condition and might be related to the formation of thermal oxides due to the austenitisation of the samples during the hot-stamping process.

Increasing the austenitisation temperature to 900 °C, but keeping the soaking time for 8 min, the coating presents three regions with different contrasts (Fig. 1 (c)), mostly related to the silicon content as seen in Fig. 2 (d). The coating matrix presents two different phases (spots 12 and 13) which mainly differ in terms of silicon content; the dark contrast of the phase represented by spot 12 shows higher silicon content than the phase pointed out in spot 13. Comparing the silicon EDS maps in Fig. 2 (c) and in Fig. 2 (d), it is seen that the thickness of the top layer enriched in silicon (6) seems to decrease (compared to the sample heated at 850 °C), being more concentrated at the outer surface (spot 12). Moreover, the silicon content in this phase (spot 12) increased from 8.8 % to 11.0 % (both % in mass fraction). Nevertheless, the highest silicon content (up to 15 % in mass fraction) is found in the brightest sublayer (spot 14), similar to the one presented in Fig. 1 (b) (spot 8). The effect of the higher austenitisation temperature is seen mainly in the thickness and in the morphology of the Fe/Si-rich sublayer (spot 14). The latter became thicker and the fraction rate of the islands decreased. Moreover, a deep crack is seen reaching the interface between the coating layer and the steel substrate. It is not possible to determine a clear interdiffusion layer. However, the interface between the coating and the steel (spot 15) presents a high iron content, aluminium and silicon in solid solution. Therefore, this region can be associated with the interdiffusion layer. Finally, an oxide layer is also observed at the coating top surface of the PHS900 sample as seen in the EDS map for oxygen in Fig. 2 (d).

The coating morphology for the samples heated at 950 °C for 8 min (laboratory scale), is the most similar to the morphologies presented in previous investigations in which the samples were produced on an industrial large scale [21,22]. It consists of five sublayers which are either enriched in aluminium (sublayers 16 and 19) or in iron/silicon (sublayers 17, 18 and 20). It is important to highlight that the Fe/Si-rich sublayers have two different contrasts: the phase in spot 17 shows a darker contrast than the phase represented by spot 18, due to the higher

silicon content in its composition. Moreover, this sample condition shows a clear interface between the coating layer and the steel substrate considered as the interdiffusion layer (21). According to the EDS semi-quantitative analysis (Fig. 2 (a)), this layer has a higher amount of iron. However, the elemental EDS map for silicon in Fig. 2 (e), shows that the silicon content is high at the interface between the coating layer and the steel substrate; and its content gradually decreases towards the steel substrate. Furthermore, a high-volume ratio of voids is seen in the coating layer. It is important to highlight that the cracks present are limited to the interdiffusion layer; and they do not reach the steel substrate. The probably reason has been attributed to the thermal expansion coefficient of the interdiffusion layer which is similar to the one of the steel [27]. Similar to the other samples' conditions, an oxide layer can be clearly seen at the surface as shown in Fig. 2 (e) (oxygen map). This oxide layer may play an important role on the corrosion mechanism as a protective barrier. However, further and dedicated research is necessary in order to fully understand the characteristics of the oxide layer. Additionally, manganese is often identified in the EDS point ID for most of the points analysed and presented (Fig. 2 (a)). This is one of the elements that comprise the steel substrate composition. The austenitisation step during hot stamping may also promote its diffusion towards the coating layer.

In general, these results show that variations in the austenitisation temperature during hot stamping can promote large changes in the morphology of the Al-Si coating. A schematic overview summarising the evolution of the Al-Si coating layer as function of different austenitisation temperatures in the hot stamping is seen in Fig. 3. This figure represents the AR sample being submitted to austenitisation temperatures (Fig. 3 (a)). The austenitisation step in hot-stamping processes takes place at temperatures higher than the melting temperature of the eutectic Al-Si alloy (577 °C) [16]. Thus, the first phenomenon which takes place during hot stamping is the melting of the aluminium alloy coating matrix, but the intermetallic phases remain in the solid state [16], as represented in Fig. 3 (b). The high temperatures during the austenitisation step promote the diffusion of the elements, mainly iron, silicon and aluminium. The former precipitates become enriched (mostly in iron) and they are rearranged forming sublayers (Fig. 3 (c–e)). The high austenitisation temperatures enhance the growth of the sublayers enriched in iron and in silicon, as represented by Fig. 3 (c–e), in which the sample heated at 950 °C shows the thicker Fe/Si-rich sublayer and a clear interdiffusion layer. Additionally, the density of defects, inherent to the hot-stamping process, is also dependent on the austenitisation temperature. Large cracks and voids were observed in the sample conditions heated at 900 °C and 950 °C. Cracks are a consequence of the thermal expansion and low fracture toughness of some brittle intermetallics. However, cracks do not reach the steel substrate and they are limited to the interdiffusion layer. The thickness of the interdiffusion layer becomes thicker as the austenitisation temperature increases. On the other hand, the voids indicate the fast diffusion between the elements [5,20,27–29]. Both cracks and voids can be detrimental to the corrosion resistance of the material.

Fan et al. [16] and Windmann et al. [19,20] have shown that the formation of intermetallics takes place in the first 2 min of the austenitisation. Furthermore, successive metallurgical transformations occur enhanced by iron enrichment. Nevertheless, they are influenced by the other hot-stamping parameters, such as soaking time and the cooling rate. The latter may have an influence suppressing the formation of stable phases. Additionally, it is important to point out that the intermetallics might originate from metastable phases. For this reason, it is rather complicated to determine the most accurate phase and/or stoichiometry by means of a semi-quantitative analysis because some of the intermetallics, mainly the ternaries of the  $\tau$ -phases (from  $\tau_1$  to  $\tau_9$ ), present very similar composition [30].

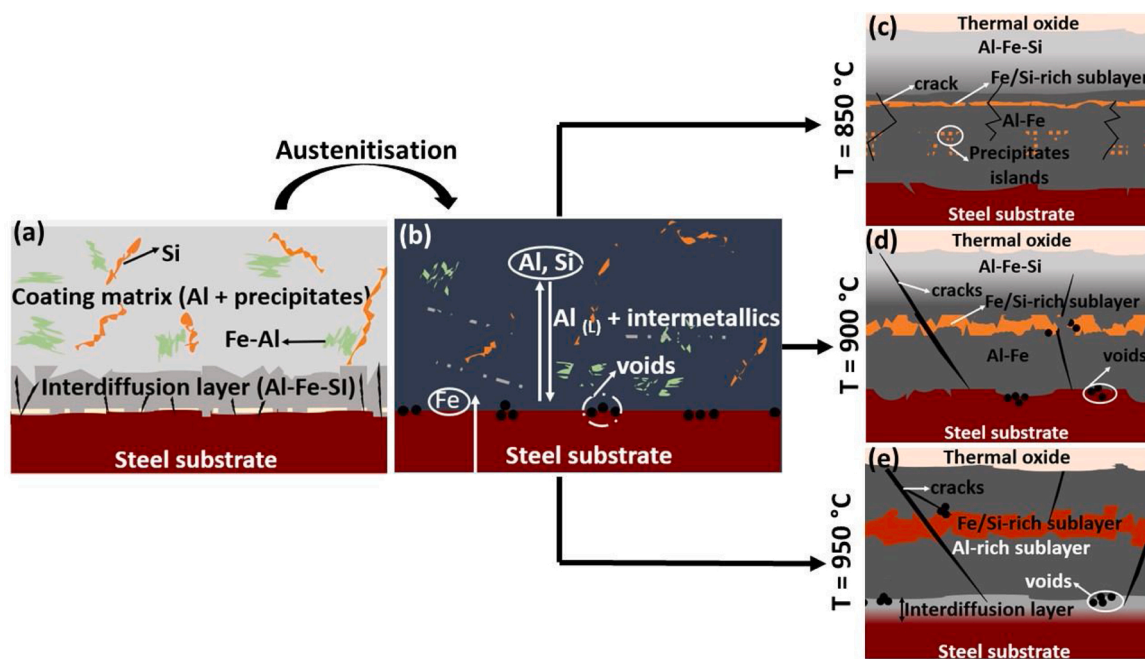


**Fig. 3.** Schematic overview representing the changes in the Al-Si coating morphology as function of temperature: (a) AR condition; (b) AR condition at austenitisation temperatures showing the melted coating layer and the solid intermetallics; (c) coating morphology austenitised at 850 °C; (d) coating morphology austenitised at 900 °C; (e) coating morphology austenitised at 950 °C.

### 3.2. Electrochemical measurements of the coated systems as function of austenitisation temperature

Fig. 4 (a) shows the *OCV* evolution during 1 h of immersion in 5% (in mass fraction) NaCl solution. The *OCV* values for both PHS900 and PHS950 decreased about 100 mV during the first 20 min of measurement. This is likely related to the dissolution of the oxide layer in contact with the electrolyte [31]. Afterwards, the potentials were kept constant. The decrease seen in the *OCV* vs. time curves of the PHS900 and PHS950 samples is rather smooth with the sole exception of a couple of spikes seen at random times. On the other hand, the PHS850 and the AR conditions show a small variation in *OCV* during the measurements, but both samples present a large number of spikes, depicted as fluctuations in the *OCV* value in a short period of time. This can be attributed to the formation of metastable pits at the sample surface, which is characteristic of Al-Si alloys [32]. After 1 h of immersion the *OCV* of all the samples were stable. The average *OCV* values for each sample condition, as well as their standard deviations, are listed in Table 2. The *OCV* of the samples is shown to increase by increasing the austenitisation

**Table 2**

Average *OCV*, *E\** and their corresponding standard deviation values for AR, PHS850, PHS900 and PHS950 samples measured in 5% NaCl solution (in mass fraction).

Sample condition	<i>OCV</i> at $t = 3600$ s (V vs Ag AgCl KCl sat.)		<i>E*</i> (V vs Ag AgCl KCl sat.)	
	Average	Standard deviation	Average	Standard deviation
AR	-0.715	0.008	-0.701	0.004
PHS850	-0.598	0.023	-0.593	0.020
PHS900	-0.583	0.008	-0.584	0.008
PHS950	-0.576	0.007	-0.578	0.007

temperature. The AR sample displays the lowest average *OCV* (-0.715 V vs Ag|AgCl|KCl sat.) whereas the PHS950 sample shows the highest average *OCV* (-0.576 V vs Ag|AgCl|KCl sat.). Furthermore, the average *OCV* values of the PHS900 and the PHS950 are very similar, and the average *OCV* difference between these samples (PHS900 and PHS950)

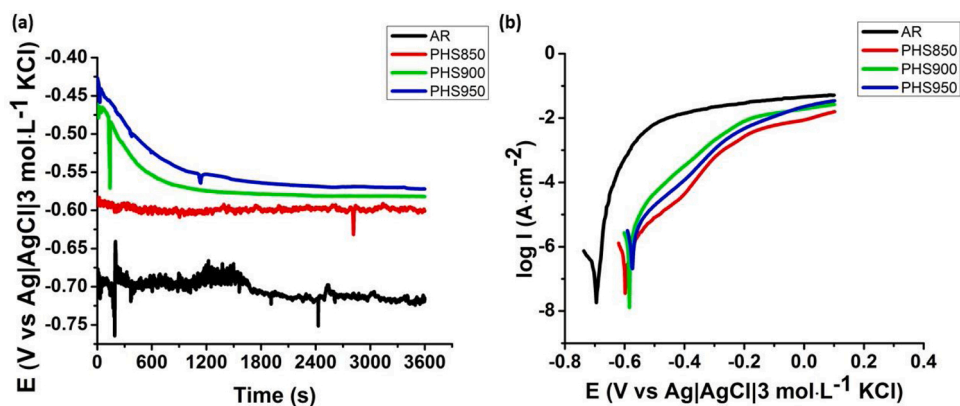


**Fig. 4.** Electrochemical measurements for AR, PHS850, PHS900 and PHS950 in 5% NaCl solution (in mass fraction): (a) open circuit potential evolution for 1 h; (b) anodic polarisation curves obtained by means of linear sweep voltammetry.

and the PHS850 is only about 20 mV. Although only a little difference is observed between the OCP values of the PHS samples, there is a trend in which the potential shifts towards nobler values by increasing the austenitisation temperature. The ennoblement of the coating layer for PHS samples was attributed in previous studies to the iron and silicon enrichment [10,21]. Nevertheless, the formed thermal oxide layer during heat treatments may also have an influence on the shifting of the OCP for the PHS samples. According to the oxygen maps shown in Fig. 2 (b–e), the oxide layer at the top coating surface of the PHS samples appears to be thicker than one at the top coating of the AR sample. Previous investigations have shown that the PHS surface consists of a mixture of iron and silicon oxides [10,20]. Therefore, the oxide layer may play a role as a protective barrier to the under-layers, increasing also the OCP values.

Fig. 4 (b) shows the characteristic anodic polarisation curves obtained just after the OCP measurement for each sample condition. An active behaviour is identified in all anodic polarisation curves. This behaviour is related to the high chloride content in the electrolyte (5% NaCl in mass fraction) which inhibits the re-passivation of the oxide layer [33]. On the other hand, a previous investigation in a less concentrated electrolyte (NaCl 0.1 mol·L<sup>-1</sup>) has shown that the surface (oxide layer) of both sample conditions AR and PHS presented a passive behaviour [22]. Table 2 also displays the average values of the corrosion potential  $E^*$  and their standard deviations.

According to Table 2, the values of  $E^*$  show the same trend as that of the OCP: the AR sample presented the lowest average  $E^*$ , while the sample heated at the highest austenitisation temperature (PHS950) shows the highest value of  $E^*$ . The average  $E^*$  difference among the austenitised samples is very small; the highest difference is 17 mV between the PHS850 and PHS950 samples. This difference increases to 107 mV when the AR and PHS950 samples are compared.

The AR sample presents the highest current density in the anodic branch ( $i_a$ ) which indicates the high susceptibility of this condition to corrosion in high chloride media (5 % NaCl in mass fraction) [33]. Moreover, an interesting difference among the anodic polarisation curves of the samples analysed is related to the current increment. For the AR sample the current increases quickly while for the PHS samples there is a relatively slower increase (see Fig. 4 (b)). This behaviour is likely to be related to the sublayers in each sample condition. As the PHS samples have the sublayers enriched in iron and silicon, this may have an influence on the current increment, because these sublayers have been pointed out as nobler than the Al-rich sublayers [21,22].

### 3.3. Scanning Kelvin probe force microscopy analysis

Fig. 5 shows the topography (a) and Volta-potential map (b), as well as a specific Volta-potential line profile (c) for the AR sample. From the topographical map (Fig. 5 (a)), it is possible to distinguish the coating layer from the steel substrate and individual precipitates in it. For the steel substrate, even some grain boundaries of the pearlite-ferrite microstructure are observed. The precipitates in the coating layer reveal a slightly higher topographical contrast.

From the Volta-potential map (Fig. 5 (b)), the interdiffusion layer can be identified at the interface of the coating layer/steel substrate. This region is not clear in the topography map (Fig. 5(a)). The Z-scale shows that the Volta potential varies approximately from -660 mV to -60 mV (vs HOPG). The darkest contrast is attributed to the free aluminium layer (see Fig. 1 (a) and Fig. 2 (b) - Al map), indicating that it is the less noble phase of the system. The precipitates and the interdiffusion layer behave cathodically versus the aluminium matrix. On the other hand, the steel substrate shows the brightest contrast, related to the noblest Volta potential.

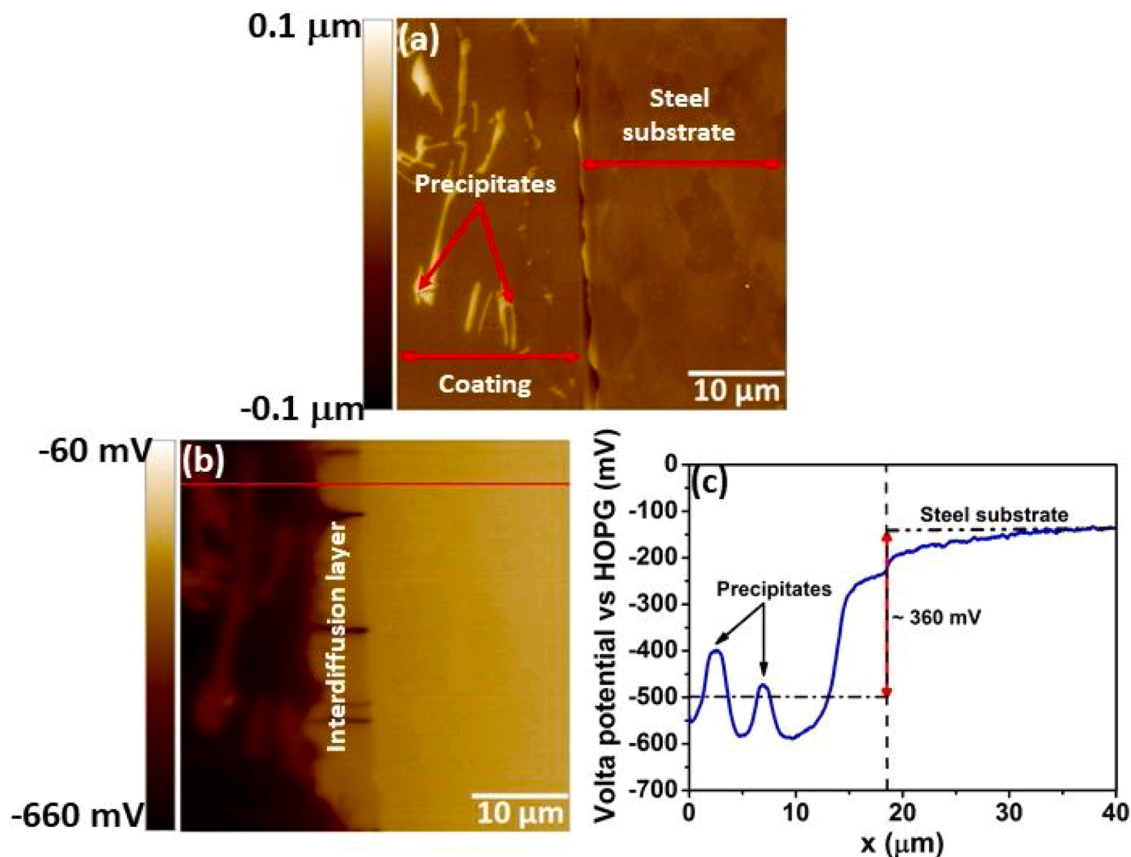


Fig. 5. Cross-section image of AR sample measured using SKPM: (a) topographic map; (b) Volta-potential map; (c) Volta-potential line profile for the line indicated in (b).

The Volta-potential line profile (Fig. 5 (c)), corresponding to the highlighted red line in Fig. 5 (b), indicates that the average Volta-potential difference between the steel substrate and the coating layer is approximately 360 mV. Moreover, the Volta potential of the precipitates in the coating layer is from 30 mV to 100 mV higher than the aluminium matrix. The average Volta potential of the interdiffusion layer is around -230 mV (vs HOPG) which is 115 mV lower than the average Volta potential of the steel substrate.

Fig. 6 shows the topography (a) and Volta-potential map (b) of the cross section of the PHS850 sample. From Fig. 6 (a), the thin sublayer and the intermetallics presented as an island morphology show higher topography than the overall coating layer which consists of different compositions along its thickness (see Fig. 1 (b) and Fig. 2 (a) - spots 6 and 7).

The Volta-potential map in Fig. 6 (b) shows the trend of the Volta potential increasing towards the steel substrate. Three different contrasts are seen in the coating layer. Correlating with Fig. 1 (b), the darkest contrast is regarding the top layer which consists of an Al-Fe-Si phase enriched in aluminium (more than 55 % in mass fraction). The thin Fe/Si-rich sublayer, highlighted in Fig. 6 (a), shows the brightest contrast of the coating layer. The contrast difference between the Fe/Si-rich sublayer, the intermetallics as islands and the Al-Fe sublayer is not very pronounced, indicating a small Volta-potential difference among them. Nonetheless, the cathodic behaviour of the steel is kept, indicated by its brightest contrast. The SKPFM results (both topography and Volta potential) show an interdiffusion layer in the sample which is nobler than the coating layer, but less noble than the bulk steel substrate. This interdiffusion layer was not easily distinguished in the backscattered electron image (Fig. 1 (b)), but it was assumed as spot10 in that same image.

Fig. 6 (c) shows the Volta-potential line profile corresponding to the

highlighted line in Fig. 6 (b). A gradient in the potential values is seen decreasing from the steel substrate to the outer surface of the coating. This can be probably related to the diffusion of iron into the coating and aluminium towards the steel substrate. Moreover, the line profile shows a great decrease in the driving force for cathodic protection (compared to the AR sample) between the coating and the steel matrix since the average Volta-potential difference between the coating layer and the steel substrate is around 100 mV. The heat treatment changed the average Volta potential of both the coating layer and the steel substrate, as they became nobler than the AR condition. The Volta-potential values of the different sublayers of the coating are distributed in a range of approximately 60 mV. Moreover, a slight peak is seen around the position  $x = 15 \mu\text{m}$ , with a potential value of approximately  $-155 \text{ mV}$  (vs HOPG) which may be attributed to the Fe/Si rich sublayer. The interdiffusion layer shows an average Volta potential of around  $-115 \text{ mV}$  (vs HOPG), only 30 mV lower than the average Volta potential of the steel substrate.

Increasing the austenitisation temperature to  $900 \text{ }^\circ\text{C}$  for 8 min, the Volta-potential of the coating/steel system significantly changes, as seen in Fig. 7.

From the Volta-potential map, Fig. 7 (b), it is seen that the Fe/Si-rich sublayers in the coating are slightly brighter than the overall coating. Additionally, a brighter and thin interdiffusion layer is seen at the interface between the coating and the steel. The steel substrate remains as the noblest phase in the system, indicating that it could be protected by cathodic protection provided by the coating layer. However, according to the Volta-potential line profile in Fig. 7 (c), for the highlighted line in Fig. 7 (b), the Volta-potential difference between the coating layer and the steel substrate decreases to 85 mV in comparison with the previous PHS850 sample. The Volta-potential values of the different sublayers of the coating are distributed in a range of

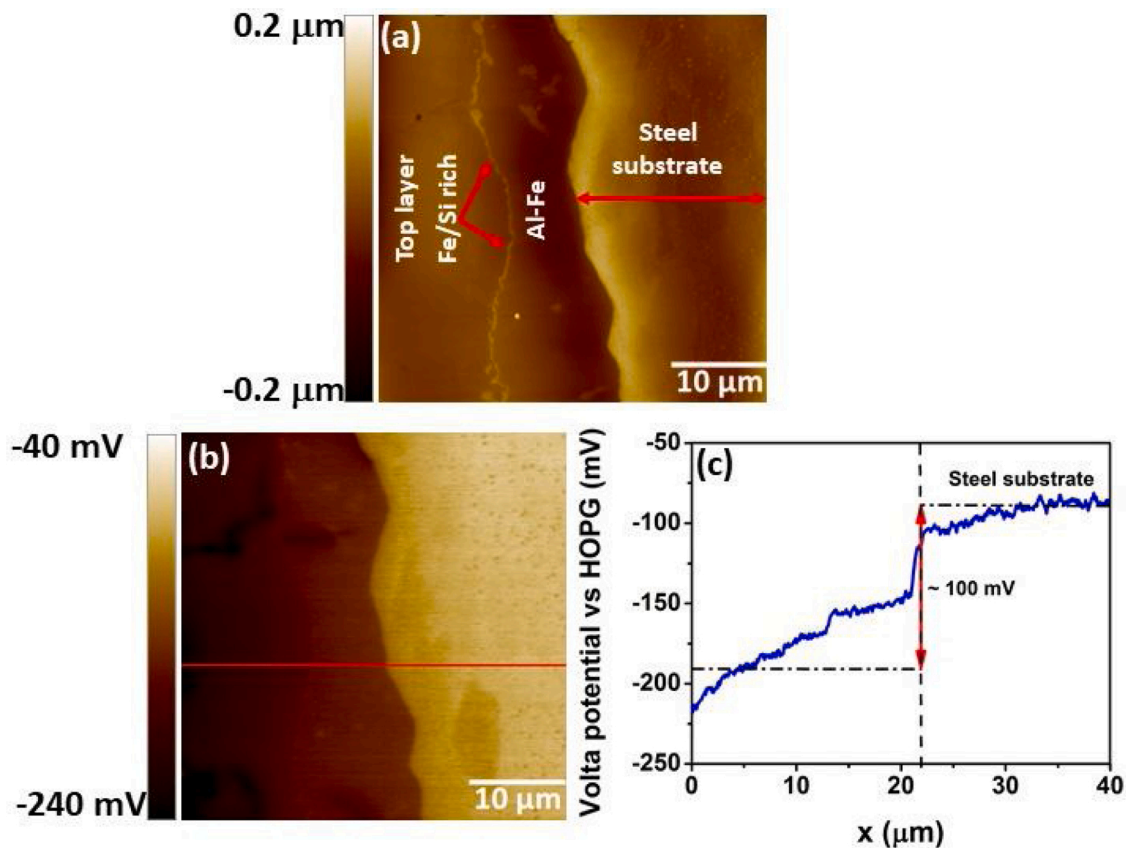


Fig. 6. Cross-section image of PHS850 sample measured by means of SKPFM: (a) topographic map; (b) Volta-potential map; (c) Volta-potential line profile for the line indicated in (b).

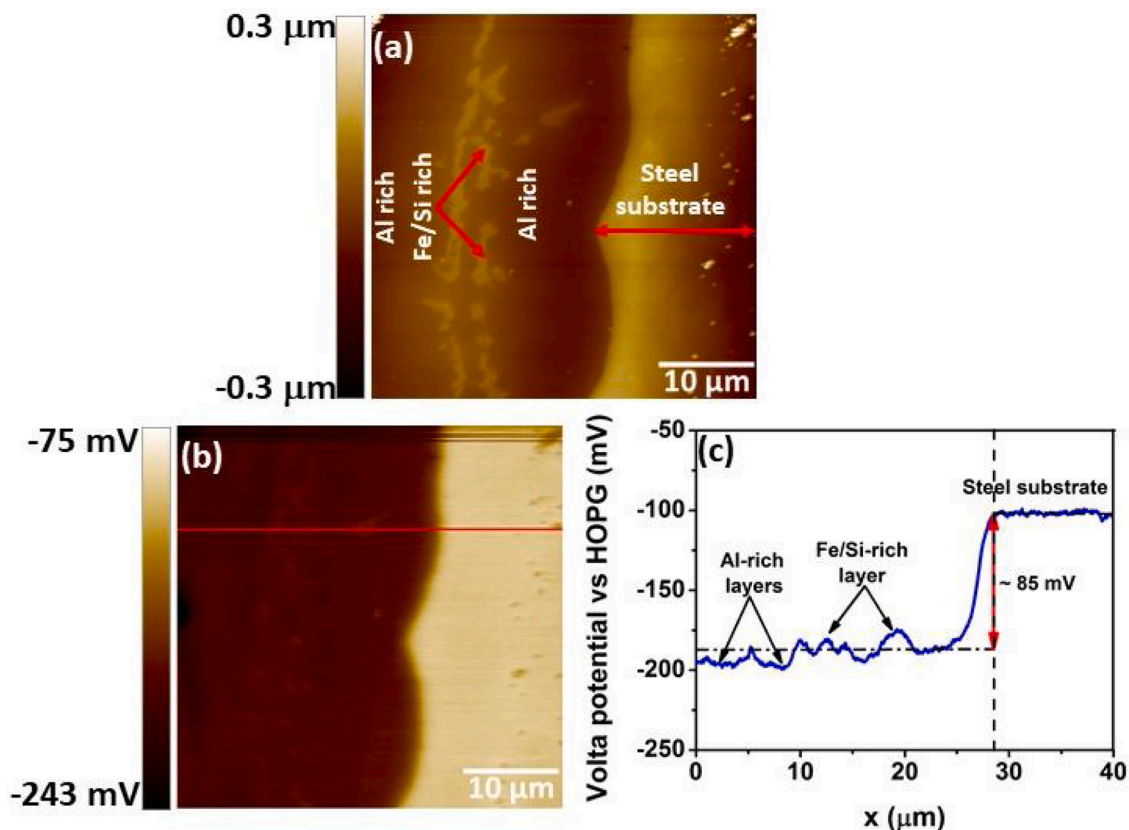


Fig. 7. Cross-section image of PHS900 sample measured by means of SKPM: (a) topographic map; (b) Volta-potential map; (c) Volta-potential line profile for the line indicated in (b).

approximately 20 mV. Additionally, the Volta potential of the interdiffusion layer is around  $-180$  mV (vs HOPG). However, this is difficult to determine as the interdiffusion layer is seen as a very thin interface. Nonetheless, these results show that increasing the austenitisation temperature, the coating layer becomes nobler and the Volta potential of the steel substrate also increases.

Fig. 8 shows the topographical map (a), the Volta-potential map (b) and a Volta-potential line profile of the PHS950 sample. The different sublayers of the coating can be clearly distinguished in the topography map of the cross section (Fig. 8 (a)).

The Volta-potential map, Fig. 8 (b), shows the brightest contrast (white) at the top surface which can probably be attributed to the thermal oxide layer, highlighted in Fig. 2 (e) - oxygen map. The coating layer shows different contrasts: the Al-rich sublayer shows the lowest Volta potential, indicated by the darkest contrast, while the Fe/Si-rich sublayer shows brighter contrast than the Al-rich sublayer. Moreover, as also seen in Fig. 1 (d), the Fe/Si-rich sublayer shows two different contrasts, indicating that one phase is nobler than another. The interdiffusion layer can be considered as the region highlighted by a rectangle, in which the Volta potential is the highest, except for the oxide layer at the top coating surface. According to the EDS mapping (Fig. 2 (e)), even though the interdiffusion layer has a high amount of iron in it, its top is enriched in silicon which justifies the highest potential. Additionally, the silicon content decreases from the coating towards the steel substrate, while the iron content is maintained. For this reason, the interdiffusion layer and the steel substrate show similar Volta-potential values.

The Volta-potential line profile in Fig. 8 (c) shows that the top layer (oxide layer) has the highest Volta potential around  $-60$  mV (vs HOPG). The Volta-potential value, of the different coating sublayers, varies in the range from approximately  $-125$  mV (Fe/Si-rich sublayers) to  $-160$  mV (Al-rich sublayers) vs HOPG. Moreover, the average Volta-potential

difference between the coating layer and the steel substrate is around 60 mV. This indicates the ennoblement of both the coating layer and the steel substrate. Additionally, Fig. 8 (c) shows that the Volta potential of the steel substrate and the interdiffusion layer is very similar, around  $-90$  mV (vs HOPG).

Fig. 9 shows the histograms constructed from the Volta-potential values obtained in the scanned areas. These histograms show the contribution of the different constituents on the Volta-potential maps [34–36]. For the AR sample, Fig. 9 (a), three different areas can be clearly distinguished: the Al matrix, the interdiffusion layer and the steel substrate. The coating layer shows a broad potential range which is related mostly to the presence of precipitates within it; while the peak observed at the lowest potential is attributed to the aluminium signal [35]. The interdiffusion layer shows a relatively sharp peak due to its homogeneity. Nonetheless, it is the steel substrate which shows the sharpest peak. However, the potential contribution of the steel substrate is not only composed of one peak due to the pearlite-ferrite microstructure. From the histogram, it is possible to estimate the average Volta-potential value of each region. It is important to highlight that these average values can be, sometimes, slightly different from those presented in the Volta-potential line profiles for each sample, because those were related to the specific line randomly chosen in the Volta-potential map. From the histograms, the average values are related to the whole scanned area. Thus, the average Volta-potential value of the Al coating matrix, the interdiffusion layer and the steel substrate are  $-480$  mV,  $-250$  mV and  $-140$  mV (vs HOPG), respectively.

Fig. 9 (b) shows the histogram of the Volta-potential values for the PHS850 sample. The coating layer is presented by two main peaks due to the different composition across the coating. The first peak around  $-180$  mV (vs HOPG) can be attributed to the top layer enriched in aluminium and the second peak, around  $-160$  mV (vs HOPG), may be related to the Al-Fe phase in which the amount of iron is around 40 % (in mass

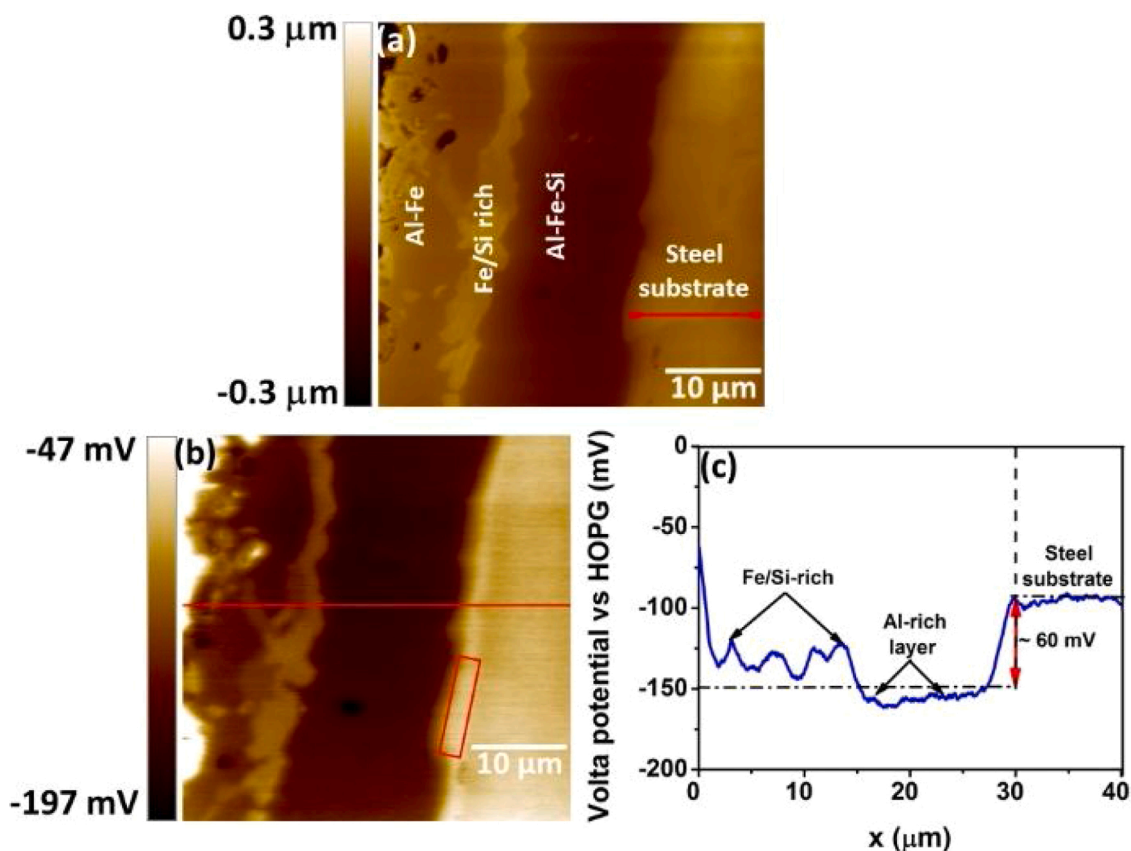


Fig. 8. Cross-section image of PHS950 sample measured by means of SKPM: (a) topographic map; (b) Volta-potential map; (c) Volta-potential line profile for the line indicated in (b).

fraction). The contribution of the Fe/Si- rich sublayer and the intermetallics cannot be precisely highlighted in the histogram as they are very thin, and the relative number of counts is very limited. Finally, the contribution from the steel substrate can be seen with an average Volta-potential of around -85 mV (vs HOPG).

The corresponding histogram for the PHS900 sample is shown in Fig. 9 (c). It presents two sharp peaks: the first at lower Volta potential regarding the coating layer and the second, at higher potentials, representing the steel substrate. It can be explained by correlation with Fig. 7 (b) which shows that the Volta potential is approximately the same throughout the whole coating layer, except for the Fe/Si-rich sublayers and the interdiffusion layer. Nevertheless, as the two latter show very thin thickness, they do not show a representative contribution in the histogram.

Fig. 9 (d) shows the histogram of the PHS950 sample. The broader area corresponds to the coating layer, as it is composed of different sublayers. The Al-rich sublayers can be characterised as the sharp peak seen at low potentials (around -150 mV vs HOPG), whereas the Fe/Si-rich sublayers show an average potential around -125 mV(vs HOPG). From Fig. 9 (by looking at the separation between the peaks) it is clear that the Volta-potential difference between the coating layer and the steel substrate decreases as the austenitisation temperature increases. Moreover, the shift towards nobler values is seen both for the coating layer and for the steel substrate. Finally, the noblest Volta potential (-60 mV vs HOPG) is attributed to the thermal oxide layer shown in Fig. 2 (c) and Fig. 8 (b).

As shown by means of the Volta-potential maps and the histograms, there is an ennoblement of the steel substrate after the thermo-mechanical process which can be attributed to the microstructural transformation from pearlite-ferrite (AR condition) into martensite (PHS samples). Fig. 10 shows the average Volta-potential value of the bulk steel substrate for each sample condition. The Volta potential of the bulk

steel substrate of each sample was measured at least three times. Thus, the box plots shown in Fig. 10 represent the merging of all the measurements. This indicates a good reproducibility for each sample condition, even considering the slight scatter. The Volta-potential values of the steel in the various PHS conditions are all in the same range; at least 25 % of potential measured are equals. Interestingly, the average Volta-potential of the steel substrate in the PHS samples is around 46 mV higher than the steel substrate in the AR condition. This is in good agreement with the value reported in our previous work (approximately 53 mV) [21]. The steel ennoblement is probably related to the microstructural transformations from pearlite-ferrite into martensite. The works of Sarkar et al. [37] and Fushimi et al. [38] show that martensite has higher corrosion potential than ferrite, which is in perfect agreement with our SKPFM results. In a dual-phase steel, ferrite acts as anode and the martensite plays the role of a cathode. On the other hand, even though martensite was shown to be nobler than ferrite, in earlier studies martensite was also reported to have a relatively higher corrosion rate compared to ferrite. According to Fushimi et al. [38] the electrochemical behaviour of the martensite is related to its supersaturated structure in carbon, as well as the residual stress involved during its microstructural transformation. The latter can alter the electronic properties of the steel matrix. This influences the Fermi level and, consequently, the work function of the material.

Fig. 11 summarises the average Volta potential of the coating layer, the steel substrate and the difference between them. This difference clearly decreases as the austenitisation temperature increases, which is an important overall observation.

As seen in Fig. 11, the higher the austenitisation temperature the lower the Volta-potential difference between the coating layer and the steel substrate. Among the austenitised samples, the PHS850 shows the highest Volta-potential difference between the coating and the steel substrate (100 mV). Moreover, as seen in Fig. 6 (c), the Volta potential

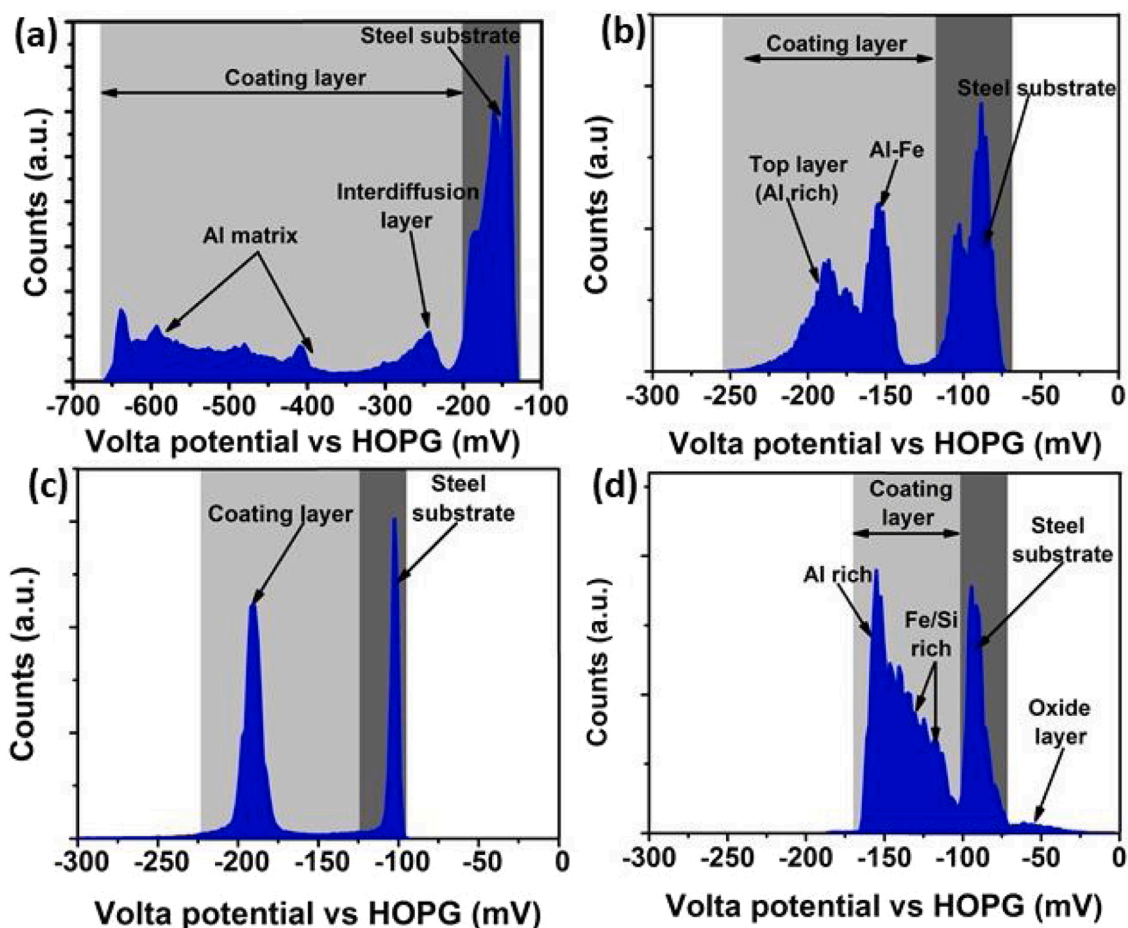


Fig. 9. Histograms based on the Volta-potential map highlighting the contribution of different phases for: (a) AR; (b) PHS850; (c) PHS900; (d) PHS950.

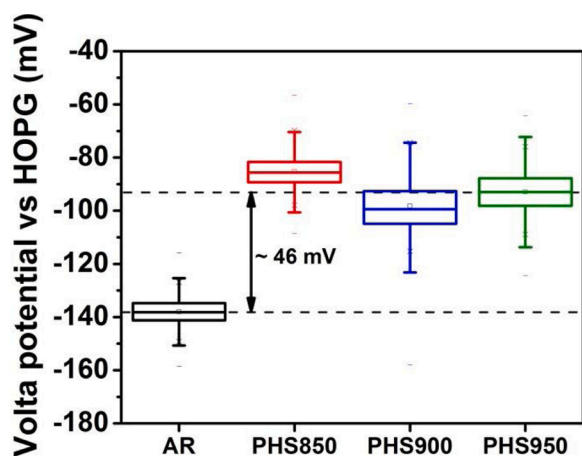


Fig. 10. Average Volta potential of the steel substrate as function of different austenitisation temperatures.

increases gradually towards the steel substrate for this sample condition. This could contribute to the reduction of galvanic-coupling effects between the steel substrate and the coating layer. The overall coating ennoblement is mainly related to iron enrichment. However, silicon plays a significant role as well, as it forms a solid solution with iron, shifting the Volta potential of the Fe/Si-rich sublayers towards nobler values [22]. On the other hand, the steel substrate becomes nobler due to the phase transformations.

The results presented here highlight the high dependence of the

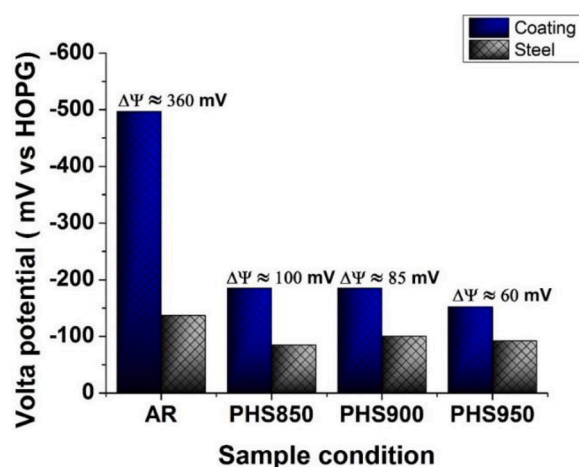


Fig. 11. Average Volta-potential of the coating layer, the steel substrate, and the difference between them ( $\Delta\Psi$ ) for each sample condition: AR, PHS850, PHS900 and PHS950.

morphology and local electrochemical behaviour of the coating/steel system on the austenitisation temperature. Increasing the austenitisation temperature causes large changes in the coating morphology, highlighted by its complexity due to the different intermetallic phases formed. Consequently, the electrochemical behaviour alters as the system (coating/steel) becomes nobler. Both global ( $E^*$  and  $OCP$ ) and local electrochemical measurements show the same trend in which the potential of the system increases as function of the austenitisation

temperature. In general, the driving force for cathodic protection is influenced by changes in austenitisation temperature, which is shown by variations in the Volta-potential difference between the steel substrate and the coating layer. Finally, as main contribution it can be said that hot-stamping austenitisation temperatures greatly alters the structure-composition of the coating and consequently changes the corrosion properties of the system.

#### 4. Conclusion

The effect of different austenitisation temperatures on the electrochemical behaviour of Al-Si coatings (10 % Si in mass fraction) was evaluated for press-hardened steels on laboratory scale. The main findings can be summarised as follows:

- i This work demonstrates that small changes in austenitisation temperature (50 °C) during the hot-stamping process can result in great variations in the Al-Si coating morphology and consequently alter the (local) electrochemical behaviour of the system (coating/steel).
- ii The hot-dip Al-Si coating becomes a multi-layered system as the austenitisation temperature increases. The increase in austenitisation temperature accelerates the diffusion of iron into the coating and promotes the formation of either binary or ternary intermetallic phases. The presence of cracks and voids is also related to higher austenitisation temperatures.
- iii Corrosion potential in NaCl solution (5% in mass fraction) shifts to nobler values by increasing the austenitisation temperature. This is attributed to the iron enrichment in the coating and the formation of thermal oxides. However, a small difference was seen between the heated (and hot stamped) samples.
- iv The Volta-potential difference between the coating layer and the steel substrate, and therefore the driving force for cathodic protection, decreases as the austenitisation temperature during the hot-stamping process increases. Both coating layer and steel substrate become nobler after the thermo-mechanical process: the first one due to the iron enrichment into the coating layer, and the second due to the phase transformation of the steel substrate from pearlite-ferrite to martensite.

#### Data availability

The raw/processed data required to reproduce these findings cannot be shared at this time as the data also forms part of an on-going study.

#### CRediT authorship contribution statement

**Camila Pucci Couto:** Conceptualization, Writing - original draft, Writing - review & editing, Visualization. **Reynier I. Revilla:** Methodology, Conceptualization, Validation, Writing - review & editing, Visualization, Supervision. **Rodolfo Politano:** Writing - review & editing. **Isolda Costa:** Writing - review & editing. **Zehbour Panossian:** Writing - review & editing. **Iris De Graeve:** Validation, Writing - review & editing. **Jesualdo Luiz Rossi:** Validation, Writing - review & editing, Visualization, Supervision. **Herman Terry:** Methodology, Validation, Writing - review & editing, Supervision.

#### Declaration of Competing Interest

The authors declare that they have no known competing financial interests or personal relationships that could have appeared to influence the work reported in this paper.

#### Acknowledgments

The authors would like to thank the Brazilian Coordination for Higher Education (CAPES), process 88881.189691/2018-01, and the

Brazilian National Council for Scientific and Technological Development (CNPq), process 205368/2018-2, for the scholarship granted to Camila Pucci Couto. In addition, the authors would like to thank Bart Lippens, for the samples cross-section preparation, and Priya Laha, for her assistance with the FE-SEM-EDS. Finally, the authors thank the companies General Motors South America, ArcelorMittal, for materials' supply and Bruning Tecnometal for the hot-stamped materials on laboratory scale.

#### References

- [1] S. Golling, D. Frómata, D. Casellas, P. Jonsén, Influence of microstructure on the fracture toughness of hot stamped boron steel, *Mater. Sci. Eng. A* 743 (2019) 529–539, <https://doi.org/10.1016/j.msea.2018.11.080>.
- [2] P. Namklang, V. Uthaisangskul, Description of microstructures and mechanical properties of boron alloy steel in hot stamping process, *J. Manuf. Process.* 21 (2016) 87–100, <https://doi.org/10.1016/j.jmapro.2015.11.008>.
- [3] C. Palm, R. Vollmer, J. Aspacher, M. Gharbi, Increasing performance of hot stamping systems, *Procedia Eng.* 207 (2017) 765–770, <https://doi.org/10.1016/j.proeng.2017.10.826>.
- [4] D.W. Fan, H.S. Kim, S. Biroasca, B.C. De Cooman, Critical review of hot stamping technology for automotive steels, *Mater. Sci. Technol.* (2007) 99–110.
- [5] D.W. Fan, B.C. De Cooman, State-of-the-knowledge on coating systems for hot stamped parts, *Steel Res. Int.* 83 (2012) 412–433, <https://doi.org/10.1002/srin.201100292>.
- [6] H. Karbasian, A.E. Tekkaya, A review on hot stamping, *J. Mater. Process. Technol.* 210 (2010) 2103–2118, <https://doi.org/10.1016/j.jmatprotec.2010.07.019>.
- [7] Y. Nakagawa, K.I. Mori, S. Yashima, T. Kaido, Springback behaviour and quenchability in hot stamping of thick sheets, *Procedia Manuf.* 15 (2018) 1071–1078, <https://doi.org/10.1016/j.promfg.2018.07.385>.
- [8] K. Mori, P.F. Bariani, B.-A. Behrens, A. Brosius, S. Bruschi, T. Maeno, M. Merklein, J. Yanagimoto, Hot stamping of ultra-high strength steel parts, *CIRP Ann. Manuf. Technol.* 66 (2017) 755–777, <https://doi.org/10.1016/j.cirp.2017.05.007>.
- [9] M. Merklein, J. Lechler, Investigation of the thermo-mechanical properties of hot stamping steels, *J. Mater. Process. Technol.* 177 (2006) 452–455, <https://doi.org/10.1016/j.jmatprotec.2006.03.233>.
- [10] C. Allély, L. Dosdat, O. Clauzeau, K. Ogle, P. Volovitch, Anticorrosion mechanisms of aluminized steel for hot stamping, *Surf. Coatings Technol.* 238 (2014) 188–196, <https://doi.org/10.1016/j.surfcoat.2013.10.072>.
- [11] L. Dosdat, J. Petitjean, T. Vietoris, O. Clauzeau, Corrosion resistance of different metallic coatings on press-hardened steels for automotive, *Steel Res. Int.* 82 (2011) 726–733, <https://doi.org/10.1002/srin.201000291>.
- [12] R. Neugebauer, F. Schieck, S. Polster, A. Mosel, A. Rautenstrauch, J. Schönherr, N. Pierschel, Press hardening - an innovative and challenging technology, *Arch. Civ. Mech. Eng.* 12 (2012) 113–118, <https://doi.org/10.1016/j.acme.2012.04.013>.
- [13] A. Deva, N.K. Jha, B.K. Jha, Effect of austenitising temperature and cooling condition on mechanical properties of low carbon boron containing steel, *Int. J. Metall. Eng.* 1 (2012) 1–6, <https://doi.org/10.5923/j.ijmee.20120101.01>.
- [14] Y. Chang, Z. Meng, L. Ying, X. Li, N. Ma, P. Hu, Influence of hot press forming techniques on properties of vehicle high strength steels, *J. Iron Steel Res. Int.* 18 (2011) 59–63, [https://doi.org/10.1016/S1006-706X\(11\)60066-6](https://doi.org/10.1016/S1006-706X(11)60066-6).
- [15] G. Venturato, M. Novella, S. Bruschi, A. Ghiotti, R. Shivpuri, Effects of phase transformation in hot stamping of 22MnB5 high strength steel, *Procedia Eng.* 183 (2017) 316–321, <https://doi.org/10.1016/j.proeng.2017.04.045>.
- [16] D.W. Fan, H.S. Kim, J.-K. Oh, K.-G. Chin, B.C. De Cooman, Coating degradation in hot press forming, *ISIJ Int.* 50 (2010) 561–568, <https://doi.org/10.2355/isijinternational.50.561>.
- [17] I. De Graeve, I. Schoukens, A. Lanzutti, F. Andreatta, A. Alvarez-Pampliega, J. De Strycker, L. Fedrizzi, H. Terry, Mechanism of corrosion protection of hot-dip aluminium-silicon coatings on steel studied by electrochemical depth profiling, *Corros. Sci.* 76 (2013) 325–336, <https://doi.org/10.1016/j.corsci.2013.07.005>.
- [18] W.-J.J. Cheng, C.-J.J. Wang, Growth of intermetallic layer in the aluminide mild steel during hot-dipping, *Surf. Coatings Technol.* 204 (2009) 824–828, <https://doi.org/10.1016/j.surfcoat.2009.09.061>.
- [19] M. Windmann, A. Röttger, W. Theisen, Formation of intermetallic phases in Al-coated hot-stamped 22MnB5 sheets in terms of coating thickness and Si content, *Surf. Coatings Technol.* 246 (2014) 17–25, <https://doi.org/10.1016/j.surfcoat.2014.02.056>.
- [20] M. Windmann, A. Röttger, W. Theisen, Phase formation at the interface between a boron alloyed steel substrate and an Al-rich coating, *Surf. Coatings Technol.* 226 (2013) 130–139, <https://doi.org/10.1016/j.surfcoat.2013.03.045>.
- [21] C.P. Couto, R.I. Revilla, M.A. Colosio, I. Costa, Z. Panossian, I. De Graeve, H. Terry, J.L. Rossi, Electrochemical behaviour of 22MnB5 steel coated with hot-dip Al-Si before and after hot-stamping process investigated by means of scanning Kelvin probe microscopy, *Corros. Sci.* 174 (2020) 108811, <https://doi.org/10.1016/j.corsci.2020.108811>.
- [22] C.P. Couto, F. Andreatta, A. Lanzutti, I. Costa, Z. Panossian, I. De Graeve, H. Terry, J.L. Rossi, R.I. Revilla, Depth profiling approach to evaluate the influence of hot stamping on the local electrochemical behaviour and galvanic series of hot-dip Al-Si coating on 22MnB5 steel, *Corros. Sci.* (2021) 109435, <https://doi.org/10.1016/j.corsci.2021.109435>.

- [23] Arcelor Mittal, Steels Coated With Alusi ®, an Aluminium-silicon Alloy Applications, 2021. <https://automotive.arcelormittal.com/products/flat/coatings/alusi>.
- [24] B. Lemmens, Y. Gonzalez Garcia, B. Corlu, J. De Strycker, I. De Graeve, K. Verbeken, Study of the electrochemical behaviour of aluminized steel, *Surf. Coatings Technol.* 260 (2014) 34–38, <https://doi.org/10.1016/j.surfcoat.2014.06.064>.
- [25] B. Lemmens, H. Springer, I. De Graeve, J. De Strycker, D. Raabe, K. Verbeken, Effect of silicon on the microstructure and growth kinetics of intermetallic phases formed during hot-dip aluminizing of ferritic steel, *Surf. Coatings Technol.* 319 (2017) 104–109, <https://doi.org/10.1016/j.surfcoat.2017.03.040>.
- [26] W.J. Cheng, C.J. Wang, Microstructural evolution of intermetallic layer in hot-dipped aluminide mild steel with silicon addition, *Surf. Coatings Technol.* 205 (2011) 4726–4731, <https://doi.org/10.1016/j.surfcoat.2011.04.061>.
- [27] Z.-X. Gui, K. Wang, Y.-S. Zhang, B. Zhu, Cracking and interfacial debonding of the Al-Si coating in hot stamping of pre-coated boron steel, *Appl. Surf. Sci.* 316 (2014) 595–603, <https://doi.org/10.1016/j.apsusc.2014.08.043>.
- [28] T. Maitra, S.P. Gupta, Intermetallic compound formation in Fe-Al-Si ternary system: part II, *Mater. Charact.* 49 (2002) 293–311, [https://doi.org/10.1016/S1044-5803\(03\)00005-6](https://doi.org/10.1016/S1044-5803(03)00005-6).
- [29] H. Springer, A. Kostka, E.J.J. Payton, D. Raabe, A. Kaysser-Pyzalla, G. Eggeler, On the formation and growth of intermetallic phases during interdiffusion between low-carbon steel and aluminum alloys, *Acta Mater.* 59 (2011) 1586–1600, <https://doi.org/10.1016/j.actamat.2010.11.023>.
- [30] S.P. Gupta, Intermetallic compound formation in Fe-Al-Si ternary system: part I, *Mater. Charact.* 49 (2003) 269–291, [https://doi.org/10.1016/S1044-5803\(03\)00006-8](https://doi.org/10.1016/S1044-5803(03)00006-8).
- [31] S. Wolyneć, *Electrochemical Techniques for Corrosion*, 1st ed., EDUSP, São Paulo, 2021, p. 176 (In Portuguese) (2033).
- [32] R.I. Revilla, J. Liang, S. Godet, I. De Graeve, Local corrosion behavior of additive manufactured AlSiMg alloy assessed by SEM and SKPFM, *J. Electrochem. Soc.* 164 (2017) C27–C35, <https://doi.org/10.1149/2.0461702jes>.
- [33] Z. Panossian, L. Mariaca, M. Morcillo, S. Flores, J. Rocha, J.J. Peña, F. Herrera, F. Corvo, M. Sanchez, O.T. Rincon, G. Pridybailo, J. Simancas, Steel cathodic protection afforded by zinc, aluminium and zinc/aluminium alloy coatings in the atmosphere, *Surf. Coatings Technol.* 190 (2005) 244–248, <https://doi.org/10.1016/j.surfcoat.2004.04.023>.
- [34] Z. Esfahani, E. Rahimi, M. Sarvghad, A. Rafsanjani-Abbasi, A. Davoodi, Correlation between the histogram and power spectral density analysis of AFM and SKPFM images in an AA7023/AA5083 FSW joint, *J. Alloys. Compd.* 744 (2018) 174–181, <https://doi.org/10.1016/j.jallcom.2018.02.106>.
- [35] M. Sarvghad-Moghaddam, R. Parvizi, A. Davoodi, M. Haddad-Sabzevar, A. Imani, Establishing a correlation between interfacial microstructures and corrosion initiation sites in Al/Cu joints by SEM-EDS and AFM-SKPFM, *Corros. Sci.* 79 (2014) 148–158, <https://doi.org/10.1016/j.corsci.2013.10.039>.
- [36] A. Davoodi, Z. Esfahani, M. Sarvghad, Microstructure and corrosion characterization of the interfacial region in dissimilar friction stir welded AA5083 to AA7023, *Corros. Sci.* 107 (2016) 133–144, <https://doi.org/10.1016/j.corsci.2016.02.027>.
- [37] P.P. Sarkar, P. Kumar, M.K. Manna, P.C. Chakraborti, Microstructural influence on the electrochemical corrosion behaviour of dual-phase steels in 3.5% NaCl solution, *Mater. Lett.* 59 (2005) 2488–2491, <https://doi.org/10.1016/j.matlet.2005.03.030>.
- [38] K. Fushimi, K. Yanagisawa, T. Nakanishi, Y. Hasegawa, T. Kawano, M. Kimura, Microelectrochemistry of dual-phase steel corroding in 0.1 M sulfuric acid, *Electrochim. Acta* 114 (2013) 83–87, <https://doi.org/10.1016/j.electacta.2013.09.162>.